Received: 15 October 2023 | Revised: 25 January 2024 | Accepted: 11 February 2024

DOI: 10.1111/jace.19778

Journal of the American Ceramic Society

RESEARCH ARTICLE

Pressure-driven homogenization of lithium disilicate glasses

Yasser Bakhouch[1] | **Silvio Buchner**[2] | **Rafael Abel Silveira**[2] | **Leonardo Resende**[2] | **Altair Soria Pereira**[2] | **Abdellatif Hasnaoui**[1] | **Achraf Atila**[3]

[1]LS2ME, Faculté Polydisciplinaire Khouribga, Sultan Moulay Slimane University of Beni Mellal, Khouribga, Morocco

[2]Graduate Program in Materials Science, Federal University of Rio Grande do Sul, Porto Alegre, Brazil

[3]Department of Material Science and Engineering, Saarland University, Saarbrücken, Germany

Correspondence
Silvio Buchner, Graduate Program in Materials Science, Federal University of Rio Grande do Sul, Porto Alegre, Brazil.
Email: silvio.buchner@ufrgs.br;

Achraf Atila, Department of Material Science and Engineering, Saarland University, Saarbrücken 66123, Germany.
Email: achraf.atila@uni-saarland.de

Funding information
Conselho Nacional de Desenvolvimento Científico e Tecnológico, Grant/Award Number: 19/2551-0001978-5; Coordenação de Aperfeiçoamento de Pessoal de Nível Superior, Grant/Award Number: 20170862; Centre National de la Recherche Scientifique et Technique, Grant/Award Number: 3USMS2022

Abstract

Lithium disilicate glasses and glass–ceramics are good potential candidates for biomedical applications, solid-state batteries, and serve as models of nucleation and crystal growth. Moreover, these glasses exhibit a phase separation that influences their nucleation and crystallization behavior. The atomistic mechanisms of the phase separation and their pressure dependence are unclear so far. Here, we used molecular dynamics simulations supported by experiments to assess the spatial heterogeneity of lithium disilicate glasses prepared under pressure. We show that the glass heterogeneity decreases with increasing the pressure under which the system was cooled and almost disappears at pressures around 30 GPa. The origin of the heterogeneity is due to the attraction between Li cations to form clustering channels, which decreases with pressure. Through our results, we hope to provide valuable insights and guidance for making glass–ceramics with controlled crystallization.

KEYWORDS

atomic structure, clustering, glass–ceramics, lithium disilicates, molecular-dynamics simulation, phase separation, X-ray diffraction

1 | INTRODUCTION

Oxide glasses are pivotal materials with a wide unique combination of properties that are pertinent for functional,[1] structural,[2] and technologically relevant applications.[3] Silicate-based glasses, as an example, are used as ultrathin substrates, strong transparent cover materials, or ion-conducting glasses.[2,3] The structure of silica glass is known to have a three-dimensional, fully connected structure made of SiO_4 tetrahedra.[4] With the addition of modifiers such as Li_2 O, the Si–O–Si bridging bonds break, and the bridging oxygen (BO) atoms are transformed to non-bridging oxygen (NBO) atoms, leading to depolymerization of the structure and a decrease of

the glass transition temperature (T_g).[5–7] The degree of depolymerization of the structure depends on the type and content of the modifier and affects the glass properties, such as mechanical and optical properties, as well as its crystallization behavior.[8–10] The control of the crystallization enabled the formation of glass–ceramics, which are materials that combine the properties of both glasses and ceramics.[11–14] These glass–ceramics have a unique combination of high strength and toughness, bioactivity, as well as excellent thermal stability. This set of properties made them useful in dental and medical applications, such as dental crowns and implants.[15,16]

The advent of glass–ceramics dates back to the 1950s in the pioneering work of Stookey,[17] wherein lithium disilicate (LS_2) served as the basis for the first glass–ceramics compositions. This discovery of glass–ceramics led to many open questions pertaining to the mechanisms underlying the nucleation and crystallization, as well as strategies for enhanced control over these processes while considering sample composition and thermal treatment.[18]

Several authors investigated the effect of processing on the properties of lithium silicate glasses and glass–ceramics. For instance, Kitamura et al.[19] studied lithium disilicate glass under high pressure using neutron diffraction and Raman scattering. They studied densification effects, particularly with lithium, comparing these glasses to pure silica. Raman spectra showed shifts in stretching and bending modes, supporting the distortion of SiO_4 tetrahedra. From the first sharp diffraction peak (FSDP), the medium-range correlation length showed a more notable decrease with volume change in lithium disilicate glass compared to pure silica. The densification was conjectured to be related to the distortion and increase in the packing density of SiO_4 tetrahedra. Voigt et al.[20] investigated the local structure and spatial distribution of lithium ions in lithium silicate glasses using nuclear magnetic resonance (NMR) and molecular dynamics (MD) simulations. Their findings indicated significant cation clustering, with stronger dipolar fields observed at the tetrahedra with three BOs, otherwise known as Q^3 sites in the Q^n notation, where n denotes the number of BO per tetrahedra, compared to Q^4 sites. MD simulations confirmed these conclusions, particularly in glasses with low lithia contents ($x = 0.10$ and 0.17), which tend to show a phase separation. Habasaki et al.[21] used MD simulations to investigate the structure of lithium disilicate glasses and melts under different pressures. Their results showed that the Q^n units changed during the compression or decompression process, with the highest percentage of Q^3 structures occurring near atmospheric pressure around T_g. These changes in the Q^n distribution were driven by variations in volume or pressure and were attributed to differences in the volumes of structural units. Recently, Bradtmüller et al.,[22] in a combined NMR and MD study, reported atomic-scale structural insights into the effect of sub-T_g annealing on the structural relaxation of LS_2 glasses. They confirmed that the arrangement of the network modifier in homogeneously nucleating glasses is closely related to those in the isochemical crystals, which was hypothesized by Zanotto et al.[23]

On the other hand, Buchner et al.,[24–27] in a series of studies, investigated the effect of processing conditions on the crystallization and properties of lithium silicate glasses using different experimental techniques. They found that processing lithium silicate glasses at high temperature and pressure increased Young's modulus and hardness by around 45% and 25%, respectively, compared to the pristine glass. Moreover, they showed that the lithium metasilicate (Li_2SiO_3) phase can form from lithium disilicate glasses if processed under high pressure and temperature. The $Li_2Si_2O_5$ phase was stable up to 6 GPa, while the Li_2SiO_3 phase began to form at 4.25 GPa and coexisted with quartz and coesite up to 6.5 GPa. The lack of lithium in the initial lithium disilicate composition led to the segregation of SiO_2 phases during the crystallization of Li_2SiO_3.[25] Another important result found in Buchner et al.[26] work is the formation of a distinctive amorphous phase of densified LS_2 glass at a pressure of 7.7 GPa, wherein small distortions on the local arrangement of the initial structure cannot be used to explain its appearance. Moreover, Resende et al.[28] showed that it is possible to produce lithium disilicate glasses at high pressure by melting and quenching them in situ at a pressure of 7.7 GPa. The results showed a significant increase in mechanical properties and completely different thermal properties compared to a reference glass sample conventionally prepared at atmospheric pressure. This was also seen as an indicative sign of the presence of polymorphism, which is the ability of the material to exist in different amorphous states.

Although experiments provided great details on the effect of processing on the structural and physical properties of lithium disilicate glasses, the atomic-scale picture of the events that govern the change in the properties is unclear. MD simulations provide quantitative and qualitative insights at the atomic scale that can be used to understand these mechanisms better. In this context, we study the effect of pressure on the densification mechanisms of lithium disilicate glasses, and we provide a detailed analysis of the glass structure at both short- and medium-range. The structural properties of the glass are compared with the experimental data of glasses similar to those prepared by Resende et al.[28] and analyzed through synchrotron X-ray diffraction (XRD).

The remainder of this paper is organized as follows. In Section 2, we describe the procedure followed to obtain the results. The calculated properties are presented in

Section 3. In Section 4, we discuss the results and suggest possible explanations for the obtained results. Concluding remarks are given in Section 5.

2 | METHODOLOGY

2.1 | Experimental procedure

Four lithium disilicate glass samples were prepared using the procedure described below. One glass batch was produced at atmospheric pressure, and the other three samples were processed under high pressure in different conditions. Standard reagent grade Li_2CO_3 (Aldrich Chem. Co. ≥ 99%) and silicon dioxide (SiO_2) (Sigma–Aldrich, ≥ 99.9%) were used to produce all samples. For the glass batch produced at atmospheric pressure, SiO_2 and Li_2CO_3 reagents were dried in a furnace for 2 h at 120° C, weighed, mixed, and melted in a Pt crucible at 1 500° C for 2 h in an electric furnace. The melt was poured on a steel plate at room temperature. Afterward, the batch was annealed at 430° C for 1 h and left to cool slowly to room temperature. This glass is called "pristine glass" in the following. Toroidal-type high-pressure apparatus was used to process samples at high pressure and high temperature (HPHT), according to the methodology described in [29–31]. The pressure was initially increased to 7.7 GPa, and then the temperature was raised to 1 873 K to melt the sample. Then, the sample was maintained at these conditions of high temperature and pressure for 10 min and subsequently quenched within 3 min while maintaining the pressure. After this procedure was done, the pressure was slowly released. Finally, after HPHT processing, the surface of the samples was grounded on SiC abrasive paper up to #1500 and polished with CeO_2 slurry for all analyses. The density of both glasses was obtained using pycnometer. The density of the pristine glass is $\rho = 2.34 \pm 0.01\ g/cm^3$ while that of the sample prepared at high-pressure is $\rho = 2.53 \pm 0.01\ g/cm^3$.

2.2 | X-ray diffraction

Transmission geometry synchrotron XRD measurements were carried out at 20 keV (λ = 0.6199 Å) on the XDS beamline of the Brazilian Synchrotron Light Laboratory (LNLS). Detection of the diffracted photons was carried out by using a standard LaBr scintillator. The powder samples were enclosed within 0.63 mm Kapton capillaries and rotated throughout the data collection to minimize grain size statistical problems. In addition to these samples, an empty capillary was also measured under the same experimental conditions in order to subtract a background that did not originate from the sample but rather from the capillary, air scattering, etc. The total structure factor $S(K)$ for an amorphous phase containing N chemical elements is derived from the normalized scattered intensity on a per-atom scale,[32,33] denoted as I_a (K), following the equations:

$$S(K) = \frac{I_a - [\langle f^2(K)\rangle - \langle f(K)\rangle^2]}{\langle f(K)\rangle^2} \quad (1)$$

$$S(K) = \sum_{i=1}^{N}\sum_{j=1}^{N} W_{ij} S_{ij}(K) \quad (2)$$

where $k = 4\pi/\lambda \sin(\theta)$ is the transferred momentum and $W_{ij}(K)$ represents the weights of the partial structure factors and can be obtained from:

$$W_{ij}(K) = W_{ji}(K) = \frac{c_i c_j f_i(K) f_j(K)}{\langle f(K)\rangle^2}, \quad (3)$$

where c_i is the concentration of i atoms and f is the atomic scattering factor and can be calculated from the prime scattering factors.[32] From the structure factor, the total pair distribution function, $G(r)$, can be calculated from a Fourier transform taking into account the atomic density, ρ_0, using the equation:

$$G(r) = 1 + \frac{1}{2\pi\rho_0 r}\int_0^{\infty} K[S(K) - 1]\sin(Kr)dK. \quad (4)$$

The $S(K)$ factors were obtained by calculating the elastic scattered intensities on a per-atom scale, normalized to electron units. This process was done after correcting the sum of elastic and inelastic scattered intensities for re-absorption effects, following the produced in ref. [34]. The inelastic scattered intensity was calculated using the analytic approximation proposed by Hajdu [35]. At the beamline, the incident radiation polarization was in the horizontal plane, whereas the data acquisition took place in the vertical plane. Thus, the polarization correction was disregarded. The form factors were obtained from the web utility available at Argonne National Laboratory website,[36] which is based on the Python software package Absorb.

2.3 | Simulation details

LAMMPS code[37] was used to perform the classic MD simulations of LS_2 glasses. The equation of motion was integrated using the velocity Verlet algorithm as implemented in LAMMPS, with a time step of 1 fs. The interactions between atoms part were modeled by the Pedone et al. potential.[38] The potential parameters and partial charges are provided in Ref. [38]. An interaction cutoff of 5.5 Å

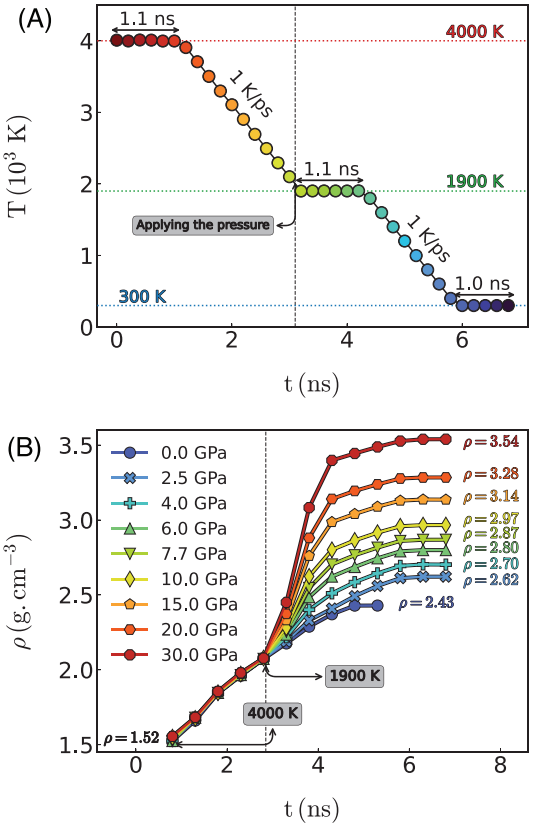

FIGURE 1 (A) The simulation profile used to obtain the glasses, (B) the evolution of density as a function of simulation time for the different prepared glasses.

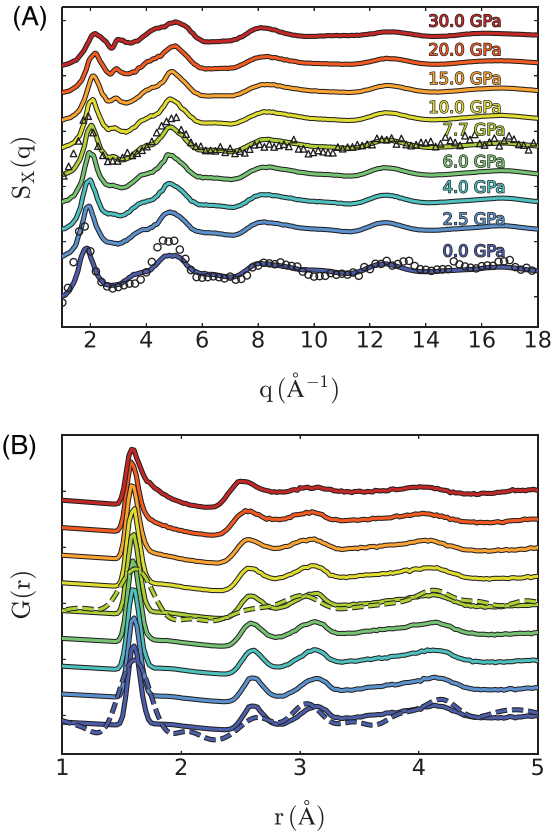

FIGURE 2 (A) X-ray diffraction structure factors for the pristine glass and all HPHT processed samples from both experiments (open symbols) and MD simulations (solid lines). (B) Calculated $G(r)$ from the structure factor data, both experiments (dashed lines) and MD simulations (solid lines). HPHT, High pressure and high temperature.

was used for short-range interactions, while the long-range interactions were treated by adopting Fennell damped shifted force (DSF) model,[39] with a damping parameter of 0.25 $Å^{-1}$ and of 8.0 Å as a long-range cutoff. This potential gives a realistic agreement with available experimental data as mentioned in the literature,[6,8,9,40–44] as it was designed to reproduce the structural and mechanical properties of a wide range of oxide glasses.

Several LS_2 glasses of stoichiometric composition $(Li_2O)_{0.33}$–$(SiO)_{0.67}$ samples were produced by randomly placing 30 000 atoms in a 3D periodic cubic simulation box while ensuring that there are no overlapping atoms. The steps followed to cool the glasses are schematically illustrated in Figure 1A and will be briefly summarized in the following. The samples were equilibrated at a high temperature (4 000 K) for 100 ps in the NVT ensemble and for 1 ns in the NPT ensemble, which was enough to make the samples lose the memory of the initial configuration. The melt was then cooled from 4 000 K to 1 900 K in NPT with zero external pressure. At 1 900 K, a pressure (P) was applied (i.e., $P = 2.5, 4, 6, 7.7, 10, 15, 20$, and 30 GPa) for 1 ns. The samples were held at the same pressure for 100 ps and then quenched to room temperature while maintaining the pressure conditions. All cooling simulations were performed using a cooling rate of 1 K/ps. After quenching, the glass was further equilibrated at 300 K in the NPT ensemble for 1 ns. Finally, we obtained seven LS_2 glasses with different densities that depend on the pressure: 2.43, 2.62, 2.70, 2.80, 2.87, 2.97, 3.14, and 3.54g/cm^3 (see Figure 1B). The simulated glasses obtained using 0 GPa and 7.7 GPa have a density that is around 3.8% and 13% higher than the glasses obtained in the experiments.

3 | RESULTS

3.1 | X-ray diffraction structure factor

Figure 2A shows the X-ray structure factor obtained from the simulated lithium disilicate glasses at different pressures. The structure factors obtained through XRD experiments for the pristine glass and the one prepared at a pressure of 7.7 GPa are shown in open symbols in the same figure for the comparison. The peak position and the

overall shape of the structure factor are well reproduced in samples prepared by MD simulations.

From the X-ray structure factor ($S_X(K)$), we obtained the total pair distribution function, $G(r)$, which was calculated and can be seen in Figure 2B, the data from the MD simulations at different pressure are also shown in the same figure. Similar to the structure factor, the $G(r)$ of the simulated glasses compares well with that obtained by XRD. It is important to remember that the simulation results were obtained under pressure, while the experimental ones were obtained at atmospheric pressure for a sample that was processed at 7.7 GPa, which causes slight differences in the peak positions.

3.2 | Neutron diffraction structure factor

The neutron structure factor of the glass prepared under zero external pressure is compared to the one measured experimentally by neutron scattering experiments from the work of Kitamura et al.,[19] and shown in Figure 3A. The structure factor of the simulated LS_2 glass at zero pressure compares well to that obtained experimentally, where the positions of the first, second, and third peaks are well reproduced at 1.78, 2.72, and 5.24 Å $^{-1}$. This good agreement highlights the interatomic potential's ability to simulate glass models with realistic glass structures. Moreover, similarities are observed in the intensity of the peaks, especially that of the FSDP in both MD and experiments. The overall shape of $S(q)$ obtained from experiments is well reproduced in the MD simulated glass structures, with slight deviations (at large q values) that can arise from the high cooling rate used in MD simulations. The pressure effect was mainly observed in the low-q region of the structure factor (see Figure 3A), which suggests that the pressure does not significantly affect the short-range structure (at least at small pressures). The shift toward higher q values of almost all peaks with increasing pressure highlights the compaction of the network as the pressure increases. It can be seen that the FSDP shifts toward high q values with increasing pressure, and its intensity decreases with increasing pressure. It is worth mentioning that this behavior of the FSDP is in good agreement with experimental observations and also results of simulated close glass compositions.[19,45–47] The FSDP, which corresponds to structural correlations on a larger length scale, was fitted using a skewed Gaussian function, and the full width at half maximum (FWHM) of the FSDP was obtained. From this FWHM, we can extract a correlation length in the medium range, allowing us to understand the correlations in the medium-range order. The correlation length was calculated using

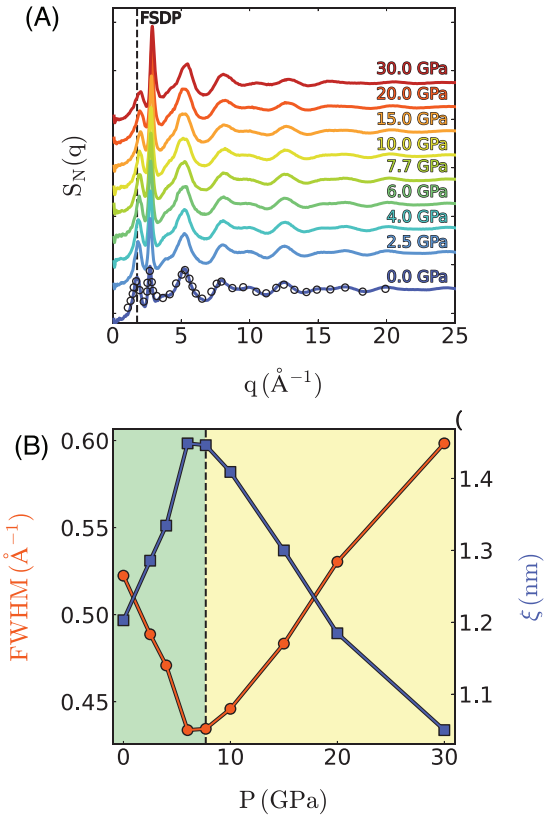

FIGURE 3 (A) Total structure factor as a function of pressure at 300 K. (B) The full width at half maximum of the first-sharp diffraction peak of the total structure factor as a function of the pressure (left y-axis) and the corresponding correlation length (right y-axis) as a function of the pressure. Error bars are smaller than the symbol size.

Equation (5)[48–51]

$$\xi = \frac{2\pi}{\mathrm{FWHM}}. \quad (5)$$

Figure 3B shows the variation of FWHM and the correlation length as a function of pressure. The FWHM increases with increasing pressure up to pressures around 6.0 GPa, then decreases to values lower than those obtained for the glass prepared under no external pressure, highlighting the possibility of polyamorphism. The correlation length behaves inversely to the FWHM. When the FWHM increases, the correlation length decreases, and vice versa. The increase in the correlation length indicates an increase in a correlated structure at the intermediate range.

3.3 | Short-range structure

The short-ranged structure of the glass is defined up to the first coordination shell of the cations with the oxygen

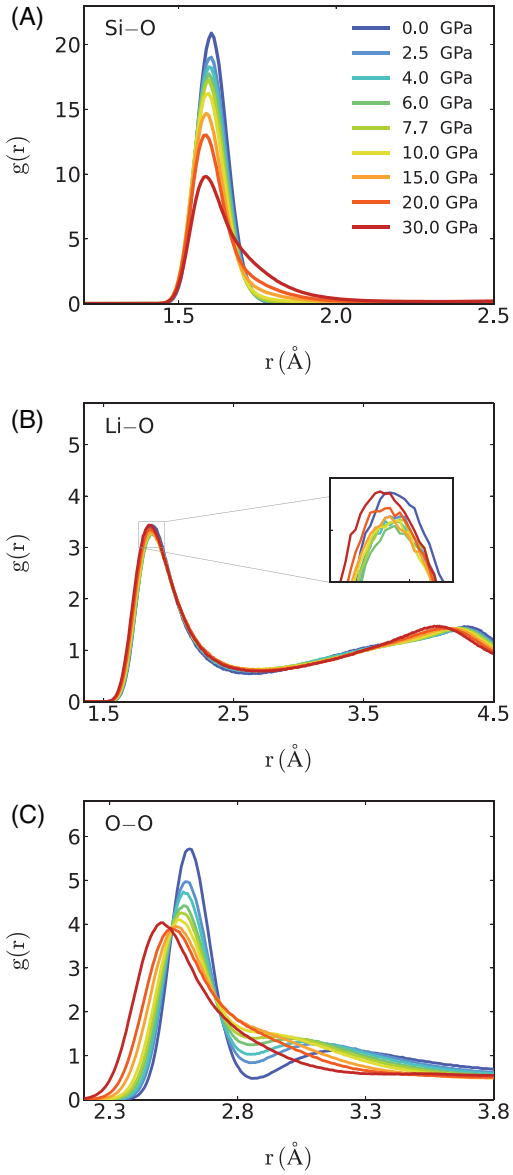

FIGURE 4 (A) Si–O, (B) Li–O, and (C) O–O partial distribution functions ($g(r)$) as a function of pressure in LS_2 glasses at 300 K.

atoms. The partial distribution function ($g(r)$) describes the short-range structure, while the location of the first peak in the $g(r)$ for the corresponding elements determines their nearest neighbor distance. Figure 4 illustrates the $g(r)$ of Si–O, Li–O, and O–O plotted up to their first minima. The first peak of Si–O pair shifts toward shorter distances, its intensity decreases, and becomes broader with increasing pressure. The Li–O $g(r)$ first peak profile showed no noticeable change with increasing pressure. The O–O $g(r)$ behaves similarly to the Si–O $g(r)$, with peaks shifting to lower r values and the first peak becoming broader.

The separation distance between Si–O, Li–O, and O–O is given in Figure 5. These bond lengths were determined

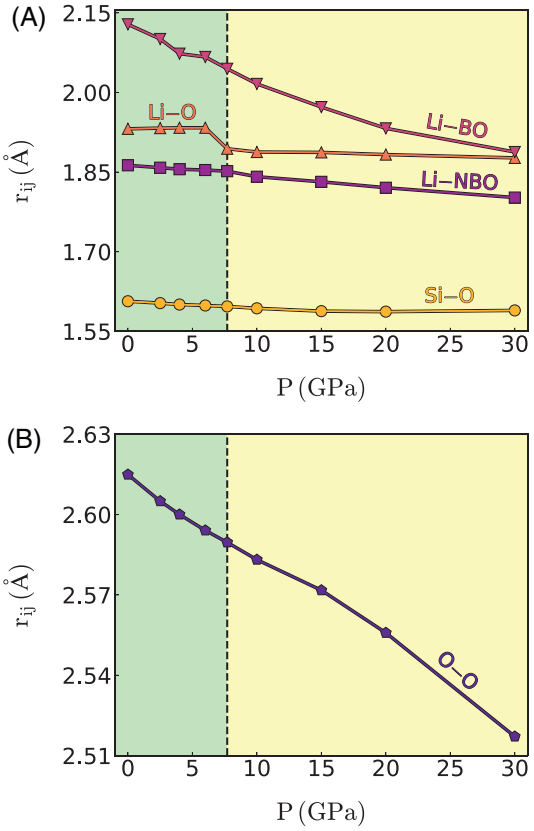

FIGURE 5 (A) Si–O and Li–O, (B) O–O bond lengths as a function of pressure in LS_2 glasses at 300 K. Error bars are smaller than the symbol size.

by fitting the first peaks of the radial probability density using the skewed-normal distribution (SND) presented in Equation (6)

$$f_{\mathrm{SND}}^{(\mu,\sigma,\zeta)}(r) = \frac{\mathrm{e}^{-(r-\mu)^2/2\sigma^2}}{\sqrt{2\pi\sigma^2}}\left[1+\mathrm{erf}\left(\zeta\frac{r-\mu}{\sqrt{2}\sigma}\right)\right], \quad (6)$$

where r is the distance between the elements, μ, σ, and ζ denote the SND coefficients. This method has been established as an efficient approach for finding the bond lengths.[52] Figure 5A shows that the Si–O bond length decreases from 1.607 Å to 1.587 Å as the pressure increases, then it increases again to 1.589 Å. The Li–O bond length is also plotted in the same figure alongside the contribution of BO and NBO to the total Li–O bond length (see Figure 5A). The Li–O bond length shows a decreasing trend with pressure, where the Li–O bond length displays a slight decrease from 1.931 to 1.876 Å, the Li–NBO bond length decreases from 1.862 to 1.802 Å, and the Li–BO bond length decreases from 2.128 Å to 1.888 Å. The O–O separation distance shown in Figure 5B displays the changes in the O–O bond length with the pressure. We notice a decrease in the separation distance between the oxygen atoms, and the change goes from 2.614 Å at 0 GPa to 2.517

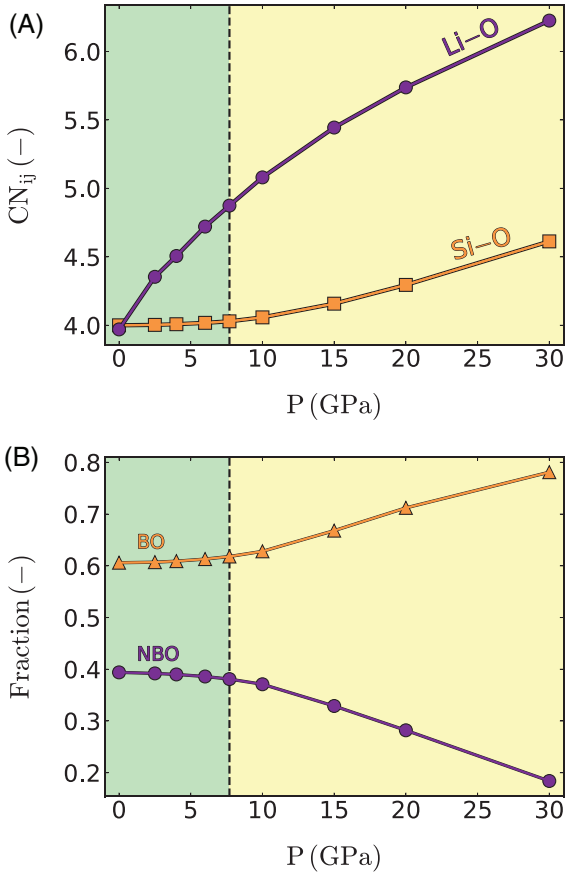

FIGURE 6 (A) Si–O and Li–O coordination numbers, (B) O–O coordination numbers, and (C) oxygen species. as a function of pressure in LS_2 glasses at 300 K. Error bars are smaller than the symbol size.

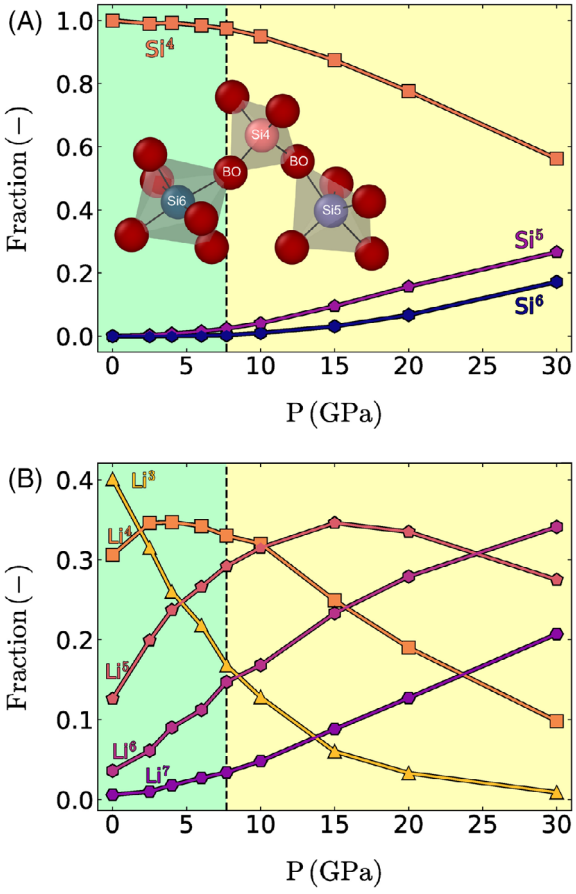

FIGURE 7 (A) Si^n coordination state, with a snapshot of 4, 5, and 6-fold coordinated Si atoms. (B) Li^n coordination state (n denotes the number of O neighbors' atoms), as a function of pressure in LS_2 glasses at 300 K. Error bars are smaller than the symbol size.

Å at 30 GPa. The CN of Si and Li atoms was found by counting the number of oxygen atoms within the first coordination shell, defined by a sphere with a radius equal to the distance where the first minimum of the $g(r)$ is found. To ensure consistency, we maintained the same radius (2.1 Å for Si–O, and 2.7 Å for Li–O) for the CN calculation at high pressures as that determined at 0 GPa. The coordination numbers show (Figure 6A) that the Si atoms have a 4-fold coordination number up to a pressure around 7.7 GPa and start increasing for pressures larger than it. At pressures lower than 7.7 GPa, most Si atoms are in a 4-fold coordination state (see Figure 7A). For pressures higher than 7.7 GPa, the amount of 5-fold and 6-fold coordinated Si atoms start to increase, with the amount of 5-fold coordinated Si atoms always being higher than the 6-fold Si atoms. The behavior of Li is different, where initially, it has a 4-fold coordination in the glass prepared without external pressure and increases rapidly with pressure (goes from 4 to 6.3). The behavior of Li^n, with n being the number of surrounding O atoms, is shown in Figure 7B. At low pressure, 3-fold and 4-fold coordination states dominate and decrease with increasing pressure, while larger coordination states appear and dominate at high pressures. From the analysis of the neighboring atoms of the oxygen, two types of oxygen atoms were distinguished, bridging oxygen (BO), which is oxygen linked to two Si atoms, and non-bridging oxygen (NBO), which is oxygen linked to only one Si atom.[8] As illustrated in Figure 6B, the dominant oxygen species in the LS_2 glass is BO, which is consistent with previous findings.[21,42,53] We also observed an increase in the fraction of BO from 60.6% up to 78.1%, and a decrease in the fraction of NBO from 39.4% to 18.4% with increasing pressure. To complement the short-range analysis depicted using the bond lengths and the coordination numbers, the bond angle distributions (BAD) will be used to gain more insight into how the pressure affected the LS_2 network topology. The BAD of O–Si–O and Si–O–Si are depicted in Figure 8. In the LS_2 glass, the O–Si–O bond angle exhibits a peak at around 109°, which is close to the ideal tetrahedral angle of ≈ 109.4°. As the pressure increases, the peak of the O–Si–O bond angle distribution shifts toward

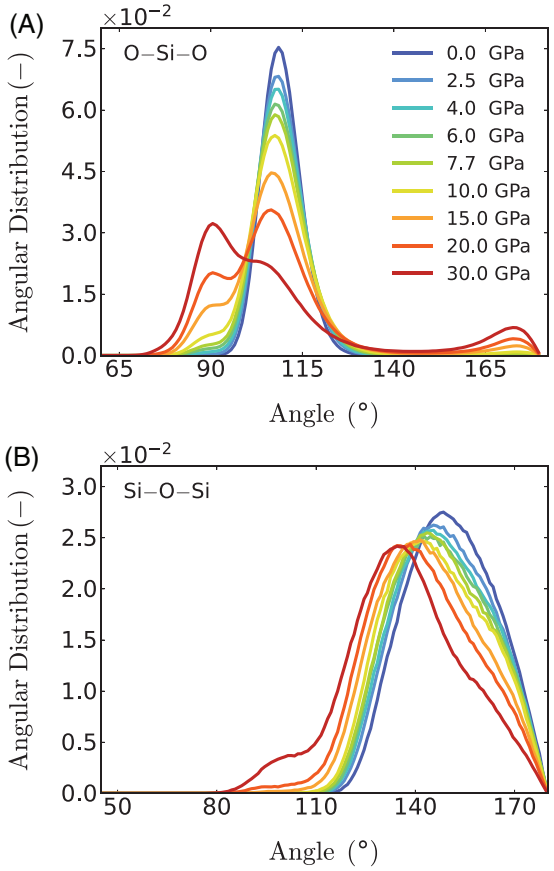

FIGURE 8 (A) O–Si–O, (B) Si–O–Si Bond angle distributions as a function of pressure in LS_2 glasses at 300 K.

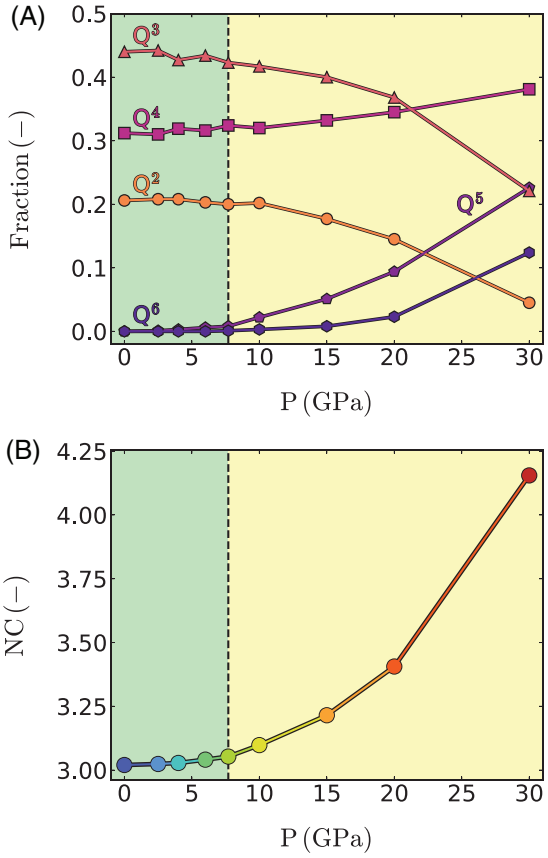

FIGURE 9 (A) Q^n distribution and (b) network connectivity as a function of pressure in LS_2 glasses at 300 K. Error bars are smaller than the symbol size.

lower angles around ≈ 106°. Also, we observed a shoulder at angles around 90° that gradually became dominant in the LS_2 glasses for the highest cooling pressure. Furthermore, smaller peaks located closer to an angle of 170° become more noticeable. The Si–O–Si BAD represents the angle between SiO_4 tetrahedra, and it has a peak at 148.5° for the glass prepared with no external pressure and decreases to 134.5° with a small shoulder appearing around 100° in the glass cooled under a pressure of 30 GPa (see Figure 8B).

3.4 | Medium-range structure

The medium-range structure of the silicate glasses can be seen as two (or more) connected Si polyhedra and highlights the connectivity of the glass. The Q^n distribution is a measure of how many BO or NBO are found in each polyhedron, where the index n refers to the number of BO atoms present in a SiO_x polyhedron. The Q^n distribution was obtained by counting how many BOs are linked to each Si polyhedron. Figure 9 depicts the evolution of Q^n percentages and the overall network connectivity (NC) of the LS_2 glasses as a function of the pressure. As pressure increases, the populations of Q^2 and Q^3 decrease while that of Q^4 increases. Additionally, Q^5 and Q^6 species significantly increase at higher pressures. Using the Q^n distribution, we can calculate the NC as the average number of BO atoms per polyhedron using Equation (7),

$$\mathrm{NC} = \sum_{i=1}^{i} n x_i \tag{7}$$

where x_i represents the fraction of Q^n species (here $n = 2$–6). The NC tends to increase with pressure, ranging from 3.02 to 4.15, indicating that the glass structure is more polymerized at larger pressure. We note that from pressure below 7.7 GPa, almost no change was observed in the Q^n population nor in the NC.

The next structural level of the medium-range order involves rings. The ring size distribution in the simulated LS_2 glasses was computed using the R.I.N.G.S code[54] based on the Guttman criterion,[55] which was shown to give a realistic ring size distribution.[5,56] The size of a given ring is described by the number of Si atoms within it. The ring size distribution for the LS_2 prepared under no pressure

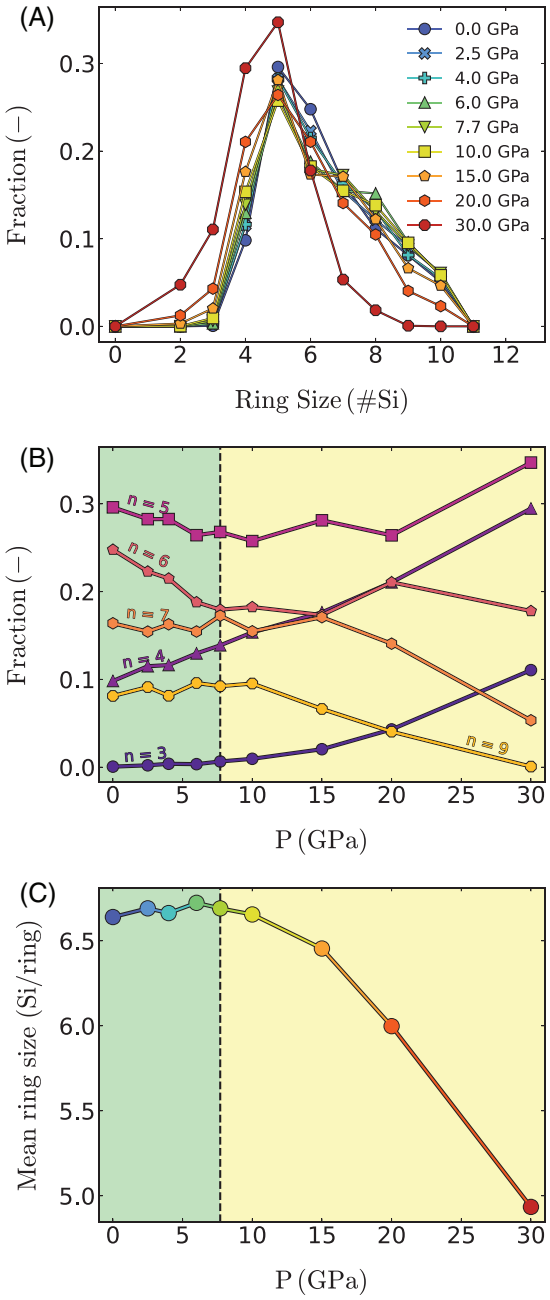

FIGURE 10 Evolution of (A) ring size distribution, (B) size of the rings, and (C) mean ring size as a function of pressure in the LS_2 glasses at 300K. Error bars are smaller than the symbol size.

(see Figure 10A) is centered around five-membered rings, which is consistent with previous findings.[42] The cooling under pressure significantly impacted the ring-size distribution. Figure 10A,B display a shift of the ring size distribution toward small ring sizes (< five-membered) while the larger ones appear to diminish. However, the mean ring size shown in Figure 10C highlights no change in the ring topology for cooling pressure under 7.7 GPa, and then the mean ring size decreases markedly at higher pressures.

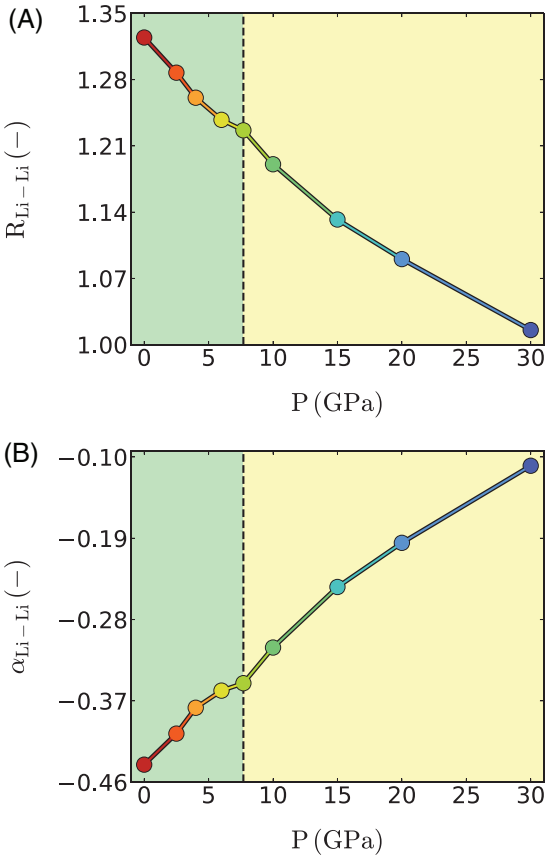

FIGURE 11 (A) The clustering ratio of Li–Li pairs and (B) chemical short-range order of Li as a function of the pressure at 300 K. Error bars are smaller than the symbol size.

3.5 | Lithium clustering

In silicate glasses, modifiers tend to cluster and form channels, which causes some phase separation in the glass. We performed an analysis using the clustering ratio,[57] calculated using Equation (8):

$$R_{\mathrm{Li-Li}} = \frac{CN_{\mathrm{Li\text{-}Li,MD}}}{CN_{\mathrm{Li\text{-}Li,hom}}} = \frac{CN_{\mathrm{Li\text{-}Li}}}{\frac{4}{3}\pi r_c^3 \frac{N_{\mathrm{Li}}}{V_{\mathrm{box}}}}, \quad (8)$$

where $R_{\mathrm{Li-Li}}$ is the clustering ratio, $CN_{\mathrm{Li\text{-}Li,MD}}$ and $CN_{\mathrm{Li\text{-}Li,hom}}$ is the Li–Li coordination number from MD simulations, and the Li–Li coordination number assuming a homogeneous distribution of Li atoms in the simulation box, respectively. N_{Li} stands for the total number of Li atoms, r_c the cutoff defined as the first minimum of the Li–Li $g(r)$ (3.8 Å), and V_{box} the volume of the simulation box. Values of $R_{\mathrm{Li-Li}}$ larger than 1 means that some clustering exists between the Li atoms. In contrast, $R = 1$ indicates a statistical distribution of Li atoms throughout the sample. The change of $R_{\mathrm{Li-Li}}$ with cooling pressure is shown in Figure 11a, where it decreases with increasing pressure. The clustering of Li atoms decreases with

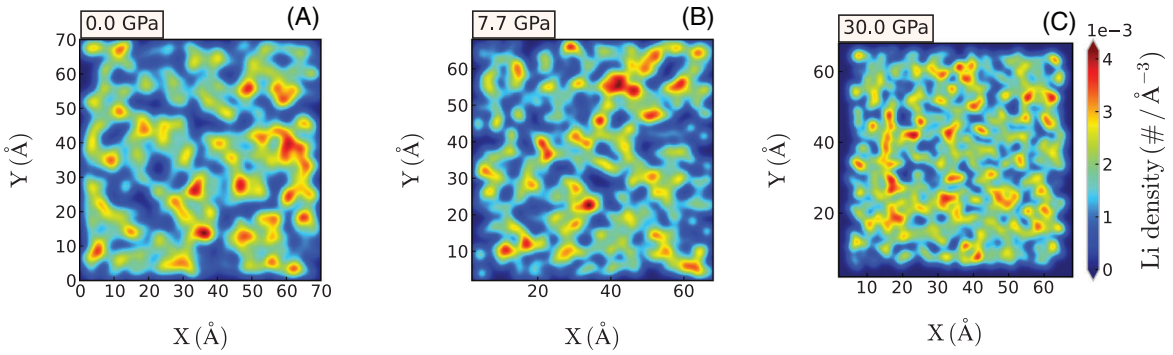

FIGURE 12 The spatial distribution of lithium density at three selected pressures in a slice of the simulation box having a width of 8 Å being twice the first minimum of the Li–Li $g(r)$. Figure S1 shows the same property as in this figure but at different locations of the simulation boxes, highlighting the generalizability of the clustering behavior and its variation with pressure.

increasing pressure. This is also highlighted visually in Figure 12, where a density map of Li atoms in a slice of the simulation box is shown for selected pressures. Figure 12 shows that in the LS_2 cooled with no external cooling pressure, clustering of Li atoms in the form of channel-like regions happens, while this clustering decreases with increasing cooling pressure.

In addition to the clustering ratio, we also computed the chemical of the short-range order (CSRO)[58] as defined in Equation (9):

$$\alpha_{i-j} = 1 - \frac{n_{i-j}}{N_i \times c_j}, \tag{9}$$

where n_{i-j} is the number of atoms of type j neighbors of a central atom of type i, N_i is the total of neighbors for the atom of type i, and c_j is the concentration of type j. Generally, this parameter ranges between −1 and 1, with negative values indicating attraction and positive values highlighting repulsion. We can see clearly that the CSRO increases with increasing pressure, indicating the homogenization tendency of the Li ions in the LS_2 glasses in our study (see Figure 11b).

4 | DISCUSSION

This study showcases the significant influence of pressure on lithium disilicate glass, as demonstrated through various analyses with changing pressure, which leads directly to a change in the glass density. Through the analysis of the structure factors, we were able to highlight that the topology of the short-range structure as depicted by the Si–O network (high q values in Figures 2 and 3) is not affected by pressures lower than or equal to 7.7 GPa, where no changes were visible in the large q regime. The change of the intensity of the FSDP and the correlation length with pressure show that we might have an amorphous–amorphous transition as an indication of polyamorphism, where we see an increase of the correlation length for cooling pressure lower than 10 GPa, and a decreasing correlation length for pressure higher than 10 GPa, which is counterintuitive if compared to metallic glasses under pressure,[48] and inline with the work of Buchner et al.[26]

We observed high dependency between the change in the SiO_x ($x = 4$–6) units and the pressure (see Figure 7). In the glass cooled with no external pressure, it can be seen that the SiO_4 units were dominant; however, at pressures higher than 7.7 GPa, the SiO_4 are still dominant, but we find a significant increase in the SiO_5 and SiO_6 units in the glass which leads to a change in the glass topology. The formation of SiO_5 and SiO_6 units can also be observed through the O–Si–O and Si–O–Si angles, where the Si–O bond lengths experience a sudden increase between 20 and 30 GPa, while the CN of Si exhibits a more gradual increasing change. Notably, the O–Si–O angles exhibit a decrease to ≈ 90°, which is indicative of the characteristic angle of an octahedron. Another notable feature of this transition is an increasing peak at 170°, which becomes more prominent at higher pressure. This transition is a common feature in the silicate glasses.[9,59–61]

With increasing pressure, the network became more polymerized, which was indicated by the formation of more BO at the cost of NBO. This repolymerization was confirmed by the increase of the NC as the pressure increased, where Q^n distributions are correlated with transformations of SiO_x units as the pressure changes. The pressure effect on the ring-size distribution in the glass could be explained by the presence of topological variation in the structure, which was related to the type of modifier present in the glass.[42,62] We notice that the mean ring size decreases with increasing pressure, indicating the dominance of small rings in the distributions; the dominance of the small rings (< 6-membered) suggests the existence of small Li-rich regions in these glasses, which we can consider it as the first indication of Li homogenization in the glasses with increasing pressure.[63–65]

The pressure-induced homogenization of the structure was shown using the clustering ratio and the density maps of the Li in the simulation box at different pressures (see Figures 11 and 12). The increase of the homogenization of the Li distribution is mainly due to an increasing repulsion between the Li atoms when the pressure increases, which is confirmed by the analysis of the CSRO parameter,[58] where for the glass cooled under no external pressure, the Li atoms are more attracted toward each other, and this attraction decreases with increasing the pressure (see Figure 11b).

5 | CONCLUSION

In conclusion, by combining experiments and MD simulations, we showed that increasing pressure significantly impacts the structure of LS_2 glasses. Polyamorphism was observed, different amorphous structures with different short- and medium-range structures, as was shown using the coordination numbers, ring statistics, and correlation lengths. Moreover, observing the oxygen species accompanied by Q^n distributions informs us that there is a high tendency for the repolmerization of the glasses as a function of the pressure. The ring size distribution suggests the existence of small Li-rich regions, which is an indicator of the homogeneity of the structure, which was shown visually through the density maps and quantitatively through the clustering ratio and CSRO. The presented results and insights into the pressure effect on the short-range order, structural unit connectivity, and homogeneity of LS_2 will help understand the glass–ceramics formation and controlled crystallization. This can enable the manipulation of the formation of specific crystalline phases and tailor the properties of the resulting glass–ceramics.

ACKNOWLEDGMENTS

Y.B. thank the Centre National de la Recherche Scientifique et Technique (CNRST) for the financial support under the agreement number (N°: 3USMS2022). S.B., R.A.S., L.R., and A.S.P. would like to thank Conselho Nacional de Desenvolvimento Científicoe Tecnológico (CNPq) and Fundação de Amparo á Pesquisa of the State of Rio Grande do Sul (FAPERGS) (project: 19/2551-0001978-5), Coordination for the Improvement of Higher Education Personnel for the financial support, and Laboratório Nacional de Luz Síncrotron (project 20170862).

Open access funding enabled and organized by Projekt DEAL.

CONFLICT OF INTEREST STATEMENT

The authors declare no conflicts of interest.

SUPPORTING INFORMATION

Additional supporting information is found in the online version of the article at the publisher's website.

ORCID

Silvio Buchner https://orcid.org/0000-0001-7939-5938
Rafael Abel Silveira https://orcid.org/0000-0001-8827-1777
Leonardo Resende https://orcid.org/0000-0003-0385-4223
Achraf Atila https://orcid.org/0000-0003-4148-5908

REFERENCES

1. Chester AM, Castillo-Blas C, Wondraczek L, Keen DA, Bennett TD. Materials formed by combining inorganic glasses and metal–organic frameworks. Chem Eur J. 2022;28(38):e202200345. Available from: https://doi.org/10.1002/chem.202200345
2. Wondraczek L, Mauro JC, Eckert J, Kühn U, Horbach J, Deubener J, et al. Towards ultrastrong glasses. Adv Mater. 2011;23(39):4578–86. Available from: https://doi.org/10.1002/adma.201102795
3. Wondraczek L, Bouchbinder E, Ehrlicher A, Mauro JC, Sajzew R, Smedskjaer MM. Advancing the mechanical performance of glasses: perspectives and challenges. Adv Mater. 2022;34(14):2109029. Available from: https://doi.org/10.1002/adma.202109029
4. Ganisetti S, Atila A, Guénolé J, Prakash A, Horbach J, Wondraczek L, et al. The origin of deformation induced topological anisotropy in silica glass. Acta Materialia. 2023;257:119108.
5. Atila A, Ghardi EM, Hasnaoui A, Ouaskit S. Alumina effect on the structure and properties of calcium aluminosilicate in the percalcic region Insights from molecular dynamics simulations. J Non Cryst Solids. 2019;525:119470. Available from: http://www.sciencedirect.com/science/article/pii/S0022309319303357
6. Atila A, Ouaskit S, Hasnaoui A. Ionic self-diffusion and the glass transition anomaly in aluminosilicates. Phys Chem Chem Phys. 2020;22(30):17205–12. Available from: https://doi.org/10.1039/d0cp02910f
7. Atila A, Bitzek E. Atomistic origins of deformation-induced structural anisotropy in metaphosphate glasses and its influence on mechanical properties. J Non-Cryst Solids. 2024;627:122822. Available from: https://www.sciencedirect.com/science/article/pii/S0022309324000024
8. Atila A, Ghardi EM, Ouaskit S, Hasnaoui A. Atomistic insights into the impact of charge balancing cations on the structure and properties of aluminosilicate glasses. Phys Rev B. 2019;100:144109. Available from: https://link.aps.org/doi/10.1103/PhysRevB.100.144109
9. Ouldhnini Y, Atila A, Ouaskit S, Hasnaoui A. Atomistic insights into the structure and elasticity of densified 45S5 bioactive glasses. Phys Chem Chem Phys. 2021;23(28):15292–301. Available from: https://doi.org/10.1039/d1cp02192c
10. Kuwik M, Pisarska J, Pisarski W. Influence of oxide glass modifiers on the structural and spectroscopic properties of phosphate glasses for visible and near-infrared photonic applications. Materials. 2020;13(10):4746.

11. Deng B, Luo J, Harris JT, Smith CM, Wilkinson TM. Toward revealing full atomic picture of nanoindentation deformation mechanisms in Li_2 O–$2SiO_2$ glass–ceramics. Acta Mater. 2021;208:116715. Available from: https://doi.org/10.1016/j.actamat.2021.116715
12. Serbena FC, Mathias I, Foerster CE, Zanotto ED. Crystallization toughening of a model glass–ceramic. Acta Mater. 2015;86:216–28. Available from: https://doi.org/10.1016/j.actamat.2014.12.007
13. Fu Q, Beall G, Smith C. Nature-inspired design of strong, tough glass-ceramics. MRS Bull. 2017;42(03):220–25.
14. Löschmann J, Fielitz P, Helsch G, Bornhöft H, Cassar DR, Borchardt G, et al. Accelerated crystal growth in a lithia aluminosilicate glass. Acta Mater. 2022;230:117837. Available from: https://doi.org/10.1016/j.actamat.2022.117837
15. Mobilio N, Catapano S. The use of monolithic lithium disilicate for posterior screw-retained implant crowns. J Prosthet Dent. 2017;118(6):703–5. Available from: https://www.sciencedirect.com/science/article/pii/S002239131730063X
16. Rodríguez-Rojas F, Óscar B-L, Sánchez-González E, Hoffman M, Guiberteau F. On the durability of zirconia-reinforced lithium silicate and lithium disilicate dental ceramics under severe contact. Wear. 2022;508–509:204460. Available from: https://www.sciencedirect.com/science/article/pii/S0043164822002186
17. Stookey SD. Catalyzed crystallization of glass in theory and practice. Ind Eng Chem. 1959;51(7):805–8. Available from: https://doi.org/10.1021/ie50595a022
18. Allix M, Cormier L. Crystallization and glass–ceramics. In: Musgraves JD, Hu J, Calvez L, editors. Cham: Springer; 2019. p. 113–67. Available from: https://doi.org/10.1007/978-3-319-93728-1_4
19. Kitamura N, Fukumi K, Mizoguchi H, Makihara M, Higuchi A, Ohno N, et al. High pressure densification of lithium silicate glasses. J Non-Cryst Solids. 2000;274(1–3):244–48. Available from: https://doi.org/10.1016/s0022-3093(00)00190-3
20. Voigt U, Lammert H, Eckert H, Heuer A. Cation clustering in lithium silicate glasses: quantitative description by solid-state NMR and molecular dynamics simulations. Phys Rev B. 2005;72:064207. Available from: https://link.aps.org/doi/10.1103/PhysRevB.72.064207
21. Habasaki J, Ngai KL. Molecular dynamics study of network statistics in lithium disilicate: Q_n distribution and the pressure–volume diagram. J Chem Phys. 2013;139(6):064503. Available from: https://doi.org/10.1063/1.4817544
22. Bradtmüller H, Gaddam A, Eckert H, Zanotto ED. Structural rearrangements during sub-T_g relaxation and nucleation in lithium disilicate glass revealed by a solid-state NMR and MD strategy. Acta Mater. 2022;240:118318. Available from: https://doi.org/10.1016/j.actamat.2022.118318
23. Zanotto ED, Tsuchida JE, Schneider JF, Eckert H. Thirty-year quest for structure–nucleation relationships in oxide glasses. Int Mater Rev. 2015;60(7):376–91. Available from: https://doi.org/10.1080/09506608.2015.1114706
24. Buchner S, Lepienski CM, Soares Jr PC, Balzaretti NM. Effect of high pressure on the mechanical properties of lithium disilicate glass ceramic. Mater Sci Eng, A. 2011;528(10):3921–24. Available from: https://www.sciencedirect.com/science/article/pii/S0921509311001171
25. Buchner S, Balzaretti NM. Pressure and temperature stability range of crystalline lithium metasilicate in a binary $Li_2O \cdot 2SiO_2$ glass. J Phys Chem Solids. 2013;74(8):1179–83. Available from: https://www.sciencedirect.com/science/article/pii/S0022369713001315
26. Buchner S, Pereira AS, de Lima JC, Balzaretti NM. X-ray study of lithium disilicate glass: high pressure densification and polyamorphism. J Non-Cryst Solids. 2014;387:112–16. Available from: https://www.sciencedirect.com/science/article/pii/S002230931400009X
27. Buchner S, Pereira AS, de Lima JC, Balzaretti NM. Effect of annealing close to T_g on the short-range order of lithium disilicate glass. J Non-Cryst Solids. 2021;560:120729. Available from: https://www.sciencedirect.com/science/article/pii/S0022309321000880
28. Resende L, Balzaretti NM, Pereira AS, Vasconcellos MAZ, Buchner S. Lithium disilicate glass produced at high pressure: characterization of structural, thermal and mechanical properties. J Am Ceram Soc. 2021;104(6):2552–59. Available from: https://doi.org/10.1111/jace.17701
29. Sherman W, Stadtmuller A. Experimental techniques in high-pressure research. Chichester: Wiley; 1987.
30. Khvostantsev LG, Slesarev VN, Brazhkin VV. Toroid type high-pressure device: history and prospects. High Pressure Res. 2004;24(3):371–83. Available from: https://doi.org/10.1080/08957950412331298761
31. Eremets M. High pressure experimental methods. Oxford University Publication; 1996.
32. Faber TE, Ziman JM. A theory of the electrical properties of liquid metals. Philos Mag. 1965;11(109):153–73. Available from: https://doi.org/10.1080/14786436508211931
33. Drewitt JWE. Liquid structure under extreme conditions: high-pressure x-ray diffraction studies. J Phys: Condens Matter. 2021;33(50):503004. Available from: https://doi.org/10.1088/1361-648X/ac2865
34. Giessen B, Wagner C. Liquid metals. In: Beer SZ, editor. Chemistry and physics. New York: Dekker; 1972.
35. Hajdu F. Analytic approximation for incoherent scattered X-ray intensities. Acta Crystallogr A. 1971;27(1):73–74. Available from: https://doi.org/10.1107/S0567739471000159
36. Argonne National Laboratory website. https://11bm.xray.aps.anl.gov/absorb/absorb.php
37. Thompson AP, Aktulga HM, Berger R, Bolintineanu DS, Brown WM, Crozier PS, et al. LAMMPS—a flexible simulation tool for particle-based materials modeling at the atomic, meso, and continuum scales. Comput Phys Commun. 2022;271:108171.
38. Pedone A, Malavasi G, Menziani MC, Cormack AN, Segre U. A new self-consistent empirical interatomic potential model for oxides, silicates, and silicas-based glasses. J Phys Chem B. 2006;110(24):11780–95.
39. Fennell CJ, Gezelter JD. Is the Ewald summation still necessary? Pairwise alternatives to the accepted standard for long-range electrostatics. J Chem Phys. 2006;124(23):234104. Available from: https://doi.org/10.1063/1.2206581
40. Atila A, Ouldhnini Y, Ouaskit S, Hasnaoui A. Atomistic insights into the mixed-alkali effect in phosphosilicate glasses. Phys Rev B. 2022;105(13):134101. Available from: https://doi.org/10.1103/physrevb.105.134101

41. Ouldhnini Y, Atila A, Ouaskit S, Hasnaoui A. Density–diffusion relationship in soda-lime phosphosilicate. J Non-Cryst Solids. 2022;590:121665. Available from: https://doi.org/10.1016/j.jnoncrysol.2022.121665
42. Atila A. Atomic structure and modifiers clustering in silicate glasses: effect of modifier cations. 2020. arXiv:200709247.
43. Ghardi EM, Atila A, Badawi M, Hasnaoui A, Ouaskit S. Computational insights into the structure of barium titanosilicate glasses. J Am Ceram Soc. 2019;102(11):6626–39. Available from: https://ceramics.onlinelibrary.wiley.com/doi/abs/10.1111/jace.16536
44. Luo J, Deng B, Vargheese KD, Tandia A, DeMartino SE, Mauro JC. Atomic-scale modeling of crack branching in oxide glass. Acta Mater. 2021;216:117098. Available from: https://doi.org/10.1016/j.actamat.2021.117098
45. Uhlig H, Hoffmann MJ, Lamparter HP, Aldinger F, Bellissent R, Steeb S. Short-range and medium-range order in lithium silicate glasses, Part I: Diffraction experiments and results. J Am Ceram Soc. 1996;79(11):2833–38.
46. Du J, Corrales LR. Compositional dependence of the first sharp diffraction peaks in alkali silicate glasses: a molecular dynamics study. J Non-Cryst Solids. 2006;352(30):3255–69. Available from: https://www.sciencedirect.com/science/article/pii/S0022309306006892
47. Le VV, Dinh HT. Structural and mechanical properties of densified (Li_2 O)0.2(SiO_2)0.8 glasses: a molecular dynamics simulations study. J Non-Cryst Solids. 2020;530:119815. Available from: https://www.sciencedirect.com/science/article/pii/S0022309319306854
48. Atila A, Kbirou M, Ouaskit S, Hasnaoui A. On the presence of nanoscale heterogeneity in $Al_{70}Ni_{15}Co_{15}$ metallic glass under pressure. J Non-Cryst Solids. 2020;550:120381. Available from: https://doi.org/10.1016/j.jnoncrysol.2020.120381
49. Krishnan NMA, Wang B, Le Pape Y, Sant G, Bauchy M. Irradiation-driven amorphous-to-glassy transition in quartz: the crucial role of the medium-range order in crystallization. Phys Rev Mater. 2017;1:053405. Available from: https://link.aps.org/doi/10.1103/PhysRevMaterials.1.053405
50. Du J, Corrales LR. First sharp diffraction peak in silicate glasses: structure and scattering length dependence. Phys Rev B. 2005;72:092201. Available from: https://link.aps.org/doi/10.1103/PhysRevB.72.092201
51. Elliott SR. Origin of the first sharp diffraction peak in the structure factor of covalent glasses. Phys Rev Lett. 1991;67:711–14. Available from: https://link.aps.org/doi/10.1103/PhysRevLett.67.711
52. Sukhomlinov SV, Müser MH. Determination of accurate, mean bond lengths from radial distribution functions. J Chem Phys. 2017;146(2):024506. Available from: https://doi.org/10.1063/1.4973804
53. Du J, Corrales LR. Structure, dynamics, and electronic properties of lithium disilicate melt and glass. J Chem Phys. 2006;125(11):114702. Available from: https://doi.org/10.1063/1.2345060
54. Le Roux S, Jund P. Ring statistics analysis of topological networks: new approach and application to amorphous GeS_2 and SiO_2 systems. Comput Mater Sci. 2010;49(1):70–83. Available from: https://www.sciencedirect.com/science/article/pii/S0927025610002363
55. Guttman L. Ring structure of the crystalline and amorphous forms of silicon dioxide. J Non-Cryst Solids. 1990;116(2):145–47. Available from: https://www.sciencedirect.com/science/article/pii/002230939090686G
56. Zhou Q, Shi Y, Deng B, Neuefeind J, Bauchy M. Experimental method to quantify the ring size distribution in silicate glasses and simulation validation thereof. Sci Adv. 2021;7(28):eabh1761. Available from: https://www.science.org/doi/abs/10.1126/sciadv.abh1761
57. Tilocca A, Cormack AN, de Leeuw NH. The structure of bioactive silicate glasses: new insight from molecular dynamics simulations. Chem Mater. 2007;19(1):95–103. Available from: https://doi.org/10.1021/cm061631g
58. Cowley JM. An approximate theory of order in alloys. Phys Rev. 1950;77:669–75. Available from: https://link.aps.org/doi/10.1103/PhysRev.77.669
59. Stebbins JF, Bista S. Pentacoordinated and hexacoordinated silicon cations in a potassium silicate glass: effects of pressure and temperature. J Non-Cryst Solids. 2019;505:234–40. Available from: https://www.sciencedirect.com/science/article/pii/S0022309318306562
60. Kapoor S, Wondraczek L, Smedskjaer MM. Pressure-induced densification of oxide glasses at the glass transition. Front Mater. 2017;4:1. Available from: https://www.frontiersin.org/articles/10.3389/fmats.2017.00001
61. Grujicic M, Bell WC, Pandurangan B, Cheeseman BA, Fountzoulas C, Patel P, et al. The effect of high-pressure densification on ballistic-penetration resistance of a soda-lime glass. Proceedings of the Institution of Mechanical Engineers, Part L. J Mater Design Appl. 2011;225(4):298–315. Available from: https://doi.org/10.1177/1464420711412849
62. Pan Z, Atila A, Bitzek E, Wondraczek L. Topology of anisotropic glasses from persistent homology analysis. J Non-Cryst Solids. 2024;627:122801. Available from: https://www.sciencedirect.com/science/article/pii/S002230932300666X
63. Du J, Cormack AN. The medium range structure of sodium silicate glasses: a molecular dynamics simulation. J Non-Cryst Solids. 2004;349:66–79. Glass Science for High Technology. 16th University Conference on Glass Science. Available from: https://www.sciencedirect.com/science/article/pii/S0022309304007963
64. Du T, Sørensen SS, To T, Smedskjaer MM. Oxide glasses under pressure: recent insights from experiments and simulations. J Appl Phys. 2022;131(17):170901. Available from: https://doi.org/10.1063/5.0088606
65. Benzine O, Pan Z, Calahoo C, Bockowski M, Smedskjaer MM, Schirmacher W, et al. Vibrational disorder and densification-induced homogenization of local elasticity in silicate glasses. Sci Rep. 2021;11(1):24454. Available from: https://doi.org/10.1038/s41598-021-04045-6

How to cite this article: Bakhouch Y, Buchner S, Silveira RA, Resende L, Pereira AS, Hasnaoui A, et al. Pressure-driven homogenization of lithium disilicate glasses. J Am Ceram Soc. 2024;107:4572–84. https://doi.org/10.1111/jace.19778